



Predicting the slowly converging dynamics of asymmetric vortex wakes

Qiang Zhong ^{1,2,*} and Daniel B. Quinn ^{2,†}¹*Department of Mechanical Engineering, Iowa State University, 2043 H.M. Black Engineering, Ames, Iowa 50011, USA*²*Department of Mechanical and Aerospace Engineering, University of Virginia, 122 Engineer's Way, Charlottesville, Virginia 22903, USA*
and Department of Electrical and Computer Engineering, University of Virginia, 122 Engineer's Way, Charlottesville, Virginia 22903, USA

(Received 26 January 2023; revised 4 August 2023; accepted 15 May 2024; published 7 June 2024)

Hydrofoils with symmetric oscillations can generate asymmetric vortex wakes. This surprising asymmetry has been widely reproduced, but a simple metric to predict its onset has remained elusive. Here, using a combination of vortex modeling and water channel experiments, we show that vortex wake deflection is well predicted by the “relative dipole angle.” In addition to offering a predictive physics-based metric, our results show that a hydrofoil’s wake can converge much slower than previously thought (more than 200 oscillation cycles), and that the wake’s asymmetry is more than a memory of the hydrofoil’s initial condition—it is an instability inherent to the vortex street.

DOI: [10.1103/PhysRevFluids.9.064702](https://doi.org/10.1103/PhysRevFluids.9.064702)

I. INTRODUCTION

When airfoils are made to oscillate in an oncoming flow, they become a simple model for a range of phenomena: from swimming fish to fluttering spoilers [1,2]. In their wake, these foils often leave a “vortex street”—a staggered array of alternating-signed vortices [3]. The streets are theoretically stable to small perturbations [4], and behind low-frequency foils, they produce time-averaged wakes that are laterally symmetric and exert no net lateral force [2].

Higher frequencies can break this lateral symmetry: wake vortices clump into pairs, and the vortex wake deflects to one side (Fig. 1). This spontaneous asymmetry has been reproduced in several experimental [5–14] and numerical [13–24] studies since it was first observed [25]. The deflection causes a net lateral force (lift) on the foil [7,11,22,23,25]; whether this lift is beneficial or detrimental depends on the application.

Prior work on wake deflection has shown that a positive “effective phase velocity” is associated with lateral asymmetry in the wake [9,18,20]. The effective phase velocity, which is a measure of the wake-induced velocity on newly shed vortex pairs, incorporates the measured flow speed, vortex spacings, and vortex strengths. This framework is useful for classifying vortex wakes, but it relies on a measured wake field, so it cannot predict wake deflection *a priori*. In contrast, a metric derived from first principles could offer a physics-based tool for predicting wake deflection.

Using a vortex model and water channel experiments, we isolated a physics-based metric—the “relative dipole angle”—that predicts vortex wake deflection. Beyond a critical relative dipole angle, the wake deflects. In our search for a metric, we also uncovered two new properties

*qzhong1@iastate.edu

†danquinn@virginia.edu

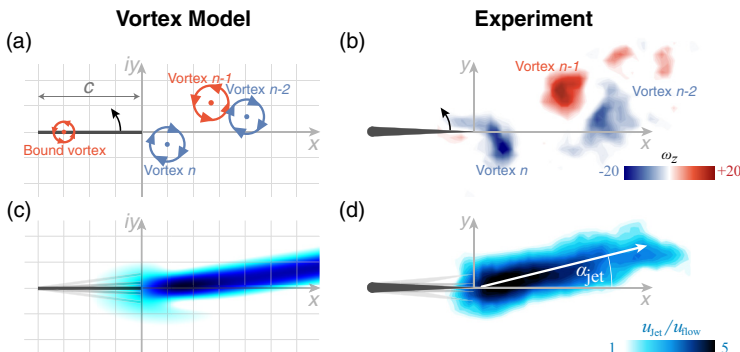


FIG. 1. Wake deflection in vortex model and experiment. (a), (b) Instantaneous wake at the midstroke of the sixth pitching cycle of the vortex model and experiment. Model: $St = 0.50$, $A = 0.25$; Experiment: $St = 0.70$, $A = 0.25$. (c), (d) Cycle-averaged flow speed of the sixth pitching cycle. Deflected jet angle α_{jct} is the angle between the horizontal axis and midline of the jet.

of wake deflection. First, just below the critical relative dipole angle, the wake converges slower than expected: deflected wakes are usually thought to converge within a few cycles [5–12,14–24], whereas we found several cases that took hundreds of cycles to converge. Second, vortex wake deflection is typically linked to the initial flapping direction [11,14,22], yet we discovered via ramp-up and ramp-down tests that vortex wake deflection is an instability inherent to the vortex street, regardless of initial conditions.

II. CLUMPED VORTEX MODEL

To model an oscillating foil’s wake we employed a form of a Brown-Michael point vortex model [26]. The model assumes an incompressible and irrotational flow governed by the “complex potential” ϕ , which is a function of position in the complex plane (z) and time (t). We will define the origin ($z = 0$) as the average position of the foil’s trailing edge [Fig. 1(a)], and we will work with a dimensionless complex potential: $\Phi(Z, T) \equiv \phi/(uc)$, where $Z \equiv z/c$ and $T \equiv t/(c/u)$, with c being the chord and u the incoming flow speed. With the system inputs being u , c , the trailing edge amplitude a , and the oscillation frequency f , the model’s dynamics are governed by two dimensionless groups, e.g., the Strouhal number, $St \equiv fa/u$ and the amplitude-to-chord ratio, $A \equiv a/c$.

Rather than capturing the full dynamics of vortex shedding, a point vortex model abstracts Φ as a superposition of uniform flow and a series of alternating-signed irrotational vortices:

$$\Phi(Z, T) = Z - i \sum_{j=0}^n \frac{\Gamma_j}{2\pi} (-1)^j \ln[Z - Z_{v,j}(T)], \quad (1)$$

where $Z_{v,j}$ is the j th vortex’s dimensionless position, Γ_j is the j th vortex’s circulation scaled by uc , and i is $\sqrt{-1}$. The $j = 0$ vortex is fixed at the quarter-chord’s average position ($Z = -0.75$) and represents bound circulation. This abstraction of the bound circulation is simpler than the more common approaches of modeling a smooth distribution of bound vortices [27,28] or using a closed-form solution for bound circulation via the Joukowski transform [29,30]; we used a single bound vortex to enable a closed-form algebraic solution for the relative dipole angle. The remaining n vortices represent circulation in the wake.

The strength and positions of the vortices are determined by the foil’s harmonic pitch oscillations. The foil’s trailing edge position is $(a/2)\cos(2\pi ft)$, so wake vortices are released at points offset from the x axis by $\pm a/2$. The j th vortex is thus released at $z = (a/2)(-1)^j i + 0.25$, with the 0.25

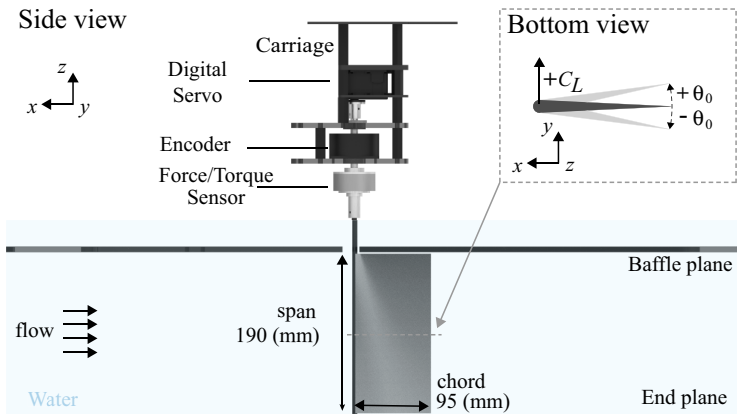


FIG. 2. Experiment setup. A nominally two-dimensional setup was achieved by installing a horizontal splitter plate and a surface plate near the tips (gap ≤ 5 mm) of a hydrofoil. The positive lift is defined as the positive direction of the y axis, and the counterclockwise direction is defined as the positive pitching direction.

horizontal offset added to avoid instabilities that arise when releasing directly at the trailing edge. The times of release correspond to times of maximum lateral velocity [$t = (1/f)(0.25 + 0.5m)$ with $m = 1, 2, 3, \dots$]. This shedding time approximates the moment when bound circulation passes through a minima or maxima, a criterion used in previous similar models [27,28,30] (see Appendix 1b for a sensitivity study). Prior to release, a wake vortex is fixed at its release point, and its strength—along with the strength of the bound vortex—is calculated using the Kutta condition (no lateral velocity at the trailing edge) and the Kelvin condition ($\sum \Gamma_j$ is constant). At the moment of release, a vortex's strength is frozen and it begins advecting via the Kirchoff velocity:

$$Z_{v,j}(T + \Delta T) = Z_{v,j}(T) + W(Z_{v,j}, T)\Delta T, \quad (2)$$

where W is the dimensionless complex velocity (complex velocity divided by u) and ΔT is the dimensionless time step used in the simulation ($\pi/12$). The complex velocity follows from a spatial derivative of the complex potential: $W(Z, T) \equiv (d\Phi/dZ)^*$ ($*$ = complex conjugate). The influence of the j th vortex is omitted when calculating the induced velocity at its own core (i.e., where $Z - Z_{v,j} = 0$). For more details on point vortex models, see, e.g., Elderidge [31] or see the Supplemental Material [32] for our step-by-step algorithm and commented source code.

We leveraged the low computational cost of this model to explore the dynamics of wake deflection over a broad range of parameters ($St = [0.34 : 0.02 : 1]$, $A = [0.25 : 0.025 : 0.45]$). Because the foil's kinematics are symmetric and the model is inviscid, the lateral added mass forces average to zero, so we used the cycle-averaged dimensionless bound vortex strength ($\bar{\Gamma}_0$) as a proxy for the lateral force experienced by the foil.

III. EXPERIMENTAL METHOD

A. Pitching hydrofoil performance measurement

In our experiments, we pitched a two-dimensional hydrofoil in a closed-loop water channel (Rolling Hills 1520, test section $380 \times 450 \times 1520$ mm, $W \times H \times L$; Fig. 2). An acrylic baffle was installed at the free surface to minimize surface waves. For all tests, the free-stream speed u was set as 71 mm s^{-1} with fluctuations less than 2.0% using an ultrasonic flowmeter (Dynasonics Series TFXB) corresponding to a Reynolds number of 6745 ($Re \equiv \rho cu/\nu$, where ρ and ν are the density and kinematic viscosities of water). We used a 190.5 mm span (s), 95-mm chord (c) hydrofoil to create a two-dimensional case by installing another horizontal splitter plate at the lower

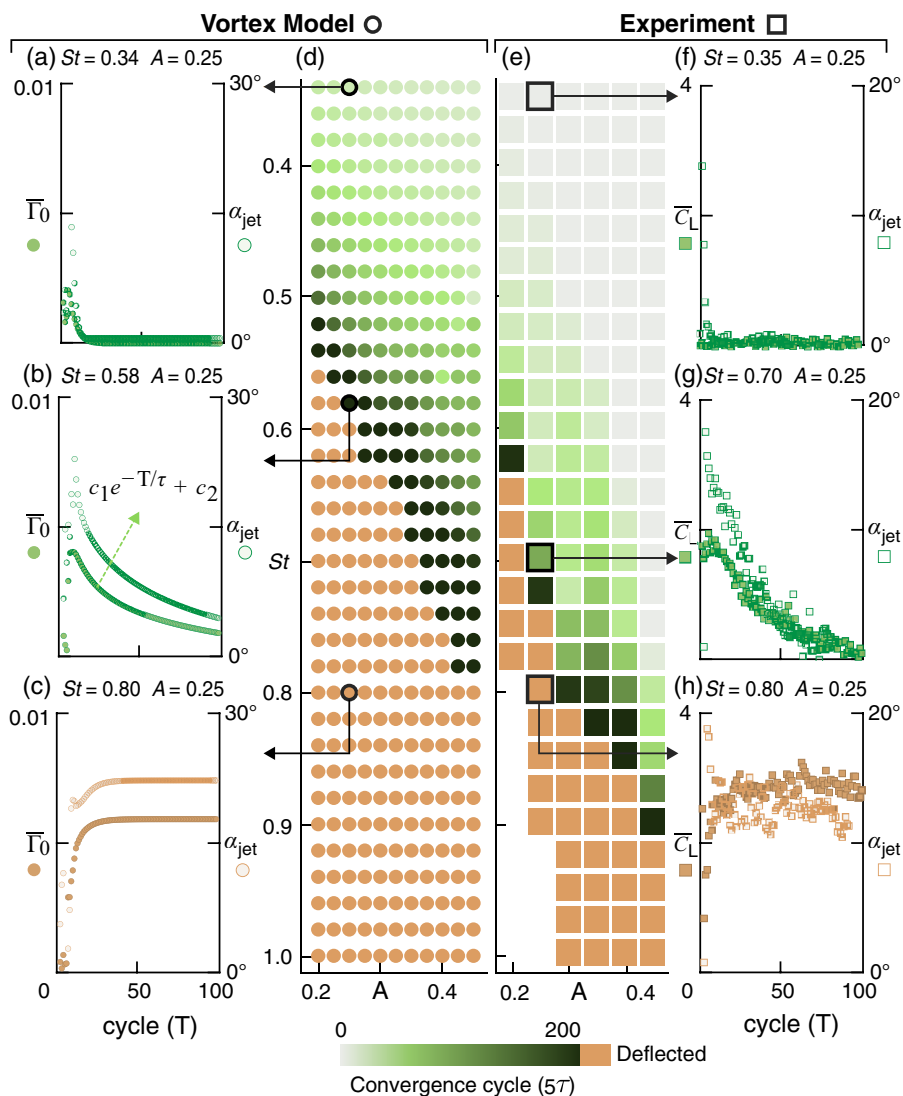


FIG. 3. The vortex model and experiments show straight and deflected wakes. Vortex model: (a)–(c) Both cycle-averaged bound vortex strength $[\bar{\Gamma}_0(T)]$ and jet angle $\alpha_{\text{jet}}(T)$ either converge to zero rapidly (a), slowly (b), or not at all (c). (d) The approximate convergence time (5τ) is a function of the Strouhal number (St) and amplitude-to-chord ratio (A). Experiments: (e)–(h) similar wake and lift convergence trends are observed. Note: results in (d) and (e) are fitted on cycle-averaged data starting from the sixth cycle and experiment results in (e) at $St = 0.375$ and 0.425 were linearly interpolated based on neighboring cases.

bottom of the hydrofoil. The gap between the tips of the hydrofoil and the baffle-splitter plate was less than 3 mm. The teardrop cross-section shape hydrofoil was 3D-printed (Stratasys F370) with Acrylonitrile Butadiene Styrene (ABS) material, and actuated by a carbon-fiber driveshaft (6.35 mm diameter) installed at its leading edge. The driveshaft was driven by a high-torque digital servo motor (Dynamixel MX64). For tests presented in Fig. 3, the pitch angle of the hydrofoil, θ , was prescribed as $\theta_0 \sin(2\pi ft)$, where θ_0 is pitch amplitude, f is frequency, and t is time.

We tested the performance of the hydrofoil over a wide range of kinematics. We considered 25 Strouhal numbers ($St \equiv 2fc \sin\theta_0/u$) between 0.35 and 1.0 and six amplitudes ($A \equiv 2c \sin\theta_0/c$) between 0.2 and 0.45 ($\theta_0 \in [5.74^\circ, 7.18^\circ, 8.63^\circ, 10.08^\circ, 11.54^\circ, 13^\circ]$). Combinations of St and A that would produce $f > 2.7$ Hz were omitted. We measured the hydrofoil’s pitching angle with an absolute encoder (US Digital A2K 4096 CPR) and forces/torques with a six-axis load cell (ATI MINI 40); both of them were installed along with the driveshaft of the hydrofoil. Then the measured forces and torques, and actual pitch angles were synchronized by a custom amplifier circuit, then packed together and transmitted to a control PC. All tests were operated and recorded by a custom LABVIEW program installed on the control PC. Each test trial was conducted five times, and the test trial consisted of five 5-s stationary periods, followed by a 200 pitching cycles. The resolution of the force-torque sensor and encoder was sufficient to resolve differences between the trials: force resolution was ± 0.005 N on the x and y axes, the torques resolution was ± 0.000125 Nm on the z axis, and the encoder’s resolution was 0.01° . We removed the bias of the sensor by subtracting the mean value of stationary measurements from the raw measurement. By coupling measured forces with angle position, we transformed raw measurements from the sensor’s local coordinate system to the water channels’ coordinate system to get net thrust (T) and lift (L). However, net-thrust performance is not discussed in this study. We reported lift measurements in nondimensional form lift coefficients $C_L \equiv L/0.5\rho scu^2$, where ρ is the density of water. The average lift coefficient within each cycle is the “cycle-averaged lift coefficient” $\bar{C}_L(T)$.

B. Flow field measurements

To explore the wake deflection convergence, we used two-dimensional plane particle image velocimetry to generate long-period flow fields. The flow was seeded with neutrally buoyant polyamide particles (20 μm average diameter), and illuminated by two opposite installed overlapping laser sheets (5 W Raypower MGL-W-532 and 10 W CNi MGL-W-532A) to avoid a hydrofoil shadow. One camera beneath the channel recorded 2956×1877 pixel images of the particle motions (Phantom, SpeedSense). Because of the limited buffer of the camera, we took ten frames per pitching cycle, therefore allowing us to take up to 100 continuous cycles of wakes. To highlight the deflection of the wake, we performed a cycle average over ten frames for each pitching cycle and quantified the jet angle (α_{jet}) between the midline of the averaged jet region and the horizontal midline (Fig. 8). Cross correlations were calculated by an adaptive particle image velocimetry (PIV) algorithm (Dantec Dynamic Studio 6.1) with 16×16 pixel overlapping interrogation windows. The cycle-averaging calculations were done in MATLAB (2022), and flow-field visualizations were generated in TECPLOT (2021R2).

IV. RESULTS

A. Model and experiments reveal slowly converging wakes

The vortex model and the experiments show similar wake convergence trends. At a fixed amplitude-to-chord ratio, low Strouhal numbers produce straight wakes and near-zero lift [Figs. 3(a) and 3(f)], while high Strouhal numbers produce deflected wakes and nonzero lift [Figs. 3(c) and 3(h)]. Wake deflection angles are comparable to those in previous experiments (e.g., $\alpha_{\text{jet}} = 13^\circ - 18^\circ$ at $St = 0.434 - 0.781$ for a heaving airfoil [7]).

Unlike previous work, kinematics between the region of low and high St led to slowly converging wake states. Wakes were deflected at first, then converged to straight slowly, sometimes over hundreds of pitch cycles. Correspondingly, the cycle-averaged lift rapidly rose, then slowly converged to zero [Figs. 3(b) and 3(g)]. In one trial of a prior model, more than 50 cycles of wake convergence were observed [13]. Prior experiments noted low-frequency deflection changes over more than 100 cycles, [5,33], but these deflection changes appear to be unrelated to the ones we observed due to their oscillatory nature. We checked by running five 1000-cycle experimental trials at $St = 0.70$ and $A = 0.25$; the cycle-averaged lift converged to zero with no sign of periodic oscillations.

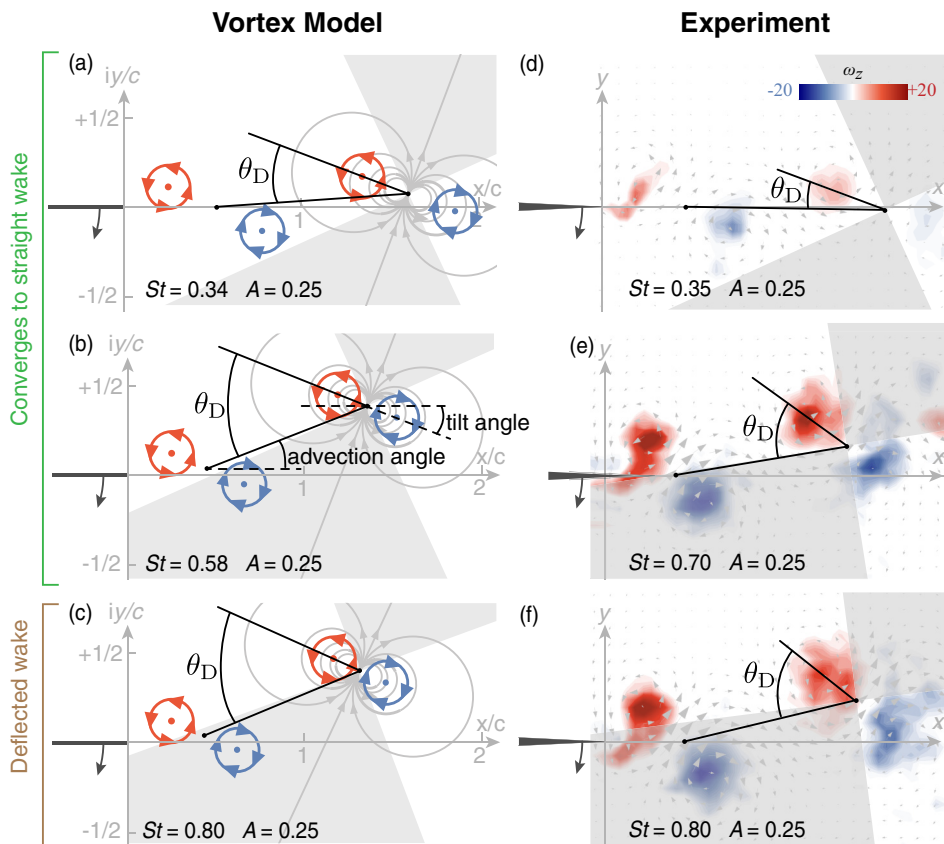


FIG. 4. The “relative dipole angle”, θ_D . (a), (d) Subcritical θ_D : dipoles have little influence on subsequent dipoles. (b), (e) Near-critical θ_D : dipoles induce slight downward velocities on subsequent dipoles, leading to a slow convergence of deflected wakes. (c), (f) Supercritical θ_D : dipoles induce upward velocities on subsequent dipoles, causing a positive feedback loop that leads to permanent wake deflection.

To quantify convergence time, we fit an exponential decay function to the $\bar{C}_L(T)$ [and $\bar{\Gamma}_0(T)$] data, i.e., we sought a function $\bar{C}_L(T) = c_1 e^{-T/\tau} + c_2$, where c_1 , c_2 , and τ are fitting coefficients. The convergence time (time until \bar{C}_L was $<1\%$ of its initial value) was approximately 5τ . Slow convergence appeared several times within the St - A space [Figs. 3(d) and 3(e)]. At low St and high A , wakes tend to be straight; as St goes up or A goes down, wakes tend to deflect perpetually; near the transition, wakes experience long convergence times. A discernible threshold between straight and deflected states appears in the St - A space of both the model and experiment [Figs. 3(d) and 3(e)]. We used our vortex model and PIV results to gain more insights into these deflection trends.

B. Relative dipole angle explains wake deflection

It has been proposed [9] that a vortex street will deflect if each vortex pair is pushed upward by preceding pairs (i.e., has a positive relative phase velocity). Our model offers a way to predict this condition *a priori*. Vortex pairs approximate a dipole in the far field, inducing upward velocities in a 90° -aperture cone centered at their core. Consequently, subsequent vortex pairs formed within this cone should generally experience upward velocities, resulting in permanently deflected wakes [Figs. 4(a)–4(c)]. This model-inspired mechanism aligns with experiments: when the centers of the

newly formed vortex pairs fell within the 90° -aperture cone, the wake tended to be permanently deflected [Figs. 4(d)–4(f)].

We hypothesized the relative dipole angle, θ_D (Fig. 4), could be a key metric for predicting wake deflection. The relative dipole angle is a sum of the previous dipole's tilt angle and its advection angle at the moment the subsequent vortex pair forms [Fig. 4(b)]. This combined angle indicates the positioning of the next vortex pair relative to the edge of the previous pair's suction cone.

Motivated by the paired structure of the vortex wake, we considered a vortex pair in isolation (i.e., the two vortices only experience induced velocities from each other and the free stream). With this simplification, the complex potential [Eq. (1)] has only a few terms, and a closed-form expression can be approximated for θ_D as follows. After the first vortex is shed, it travels approximately $u/(2f)$ downstream before the second vortex is shed. In dimensionless distance, it has traveled $A/(2St)$. The dimensionless distance from one vortex to the other is therefore $A[i - 1/(2St)]$, and the induced dimensionless complex velocity on the vortex pair is

$$W_{\text{dipole}} = \left(1 + \frac{i}{2\pi} \frac{\Gamma_j}{A[i - 1/(2St)]} \right)^* \quad (3)$$

$$\approx 1 + \frac{St^2}{A(i/2 - St)}. \quad (4)$$

The approximation above makes use of the fact that $\Gamma_j/(2\pi) \sim St$. One can show this by considering that a typical lateral speed of the airfoil is af and a typical speed induced on the foil by the j th vortex as it sheds is $u * \Gamma_j/(2\pi)$. To ensure the Kutta condition, these two velocities must balance, meaning that $\Gamma_j/(2\pi) \sim af/u = St$.

The relative dipole angle's first component, the tilt angle, follows from the relative positioning of the vortex pair and is equal to $\text{Arg}[A/(2St) + Ai]$. The second component, the advection angle, is the argument of the induced complex velocity of the vortex pair, $\text{Arg}[W_{\text{dipole}}]$. The relative dipole angle can thus be estimated as

$$\theta_D \approx \arg \left[\left(1 + \frac{St^2}{A(i/2 - St)} \right) \right] + \arg \left[\frac{A}{2St} + Ai \right] \quad (5)$$

Assuming small angles ($\arg[Z] \approx \text{Im}[Z]/\text{Re}[Z]$) and small Strouhal numbers ($1 + St^2 \approx 1$), this expression reduces to

$$\theta_D \sim St \left(1 + \frac{2St}{A} \right), \quad (6)$$

where leading coefficients have been dropped, because we seek a scaling for θ_D rather than a prediction of its value. In theory, beyond some critical value of $St(1 + 2St/A)$, new vortex pairs should shed within the 90° -aperture cone [Fig. 4(c)] and be induced upward in the reference frame of the previous pair.

Wake deflection appears to be well predicted by our scaling for the relative dipole angle. Increasing $St(1 + 2St/A)$ causes τ to rise from zero, then become infinite [no convergence; Figs. 5(a) and 5(b)]. At least for harmonically pitched hydrofoils, the relative dipole angle appears to be a useful physics-based metric for predicting wake deflection, or the wake convergence time when wakes decay to zero angles. As a comparison, we also plotted τ against two control metrics. The first is an estimate of the dimensionless effective phase velocity, taken as the imaginary part of W_{dipole} in Eq. (4). This criteria does not effectively predict deflection [Figs. 5(c) and 5(d)]. Presumably the assumptions in our model compromise this metric's accuracy, despite its effectiveness when applied to measured velocity fields [9,18,20]. The second is the Strouhal number, which does not capture amplitude effects and therefore does not effectively predict deflection [Figs. 5(e) and 5(f)].

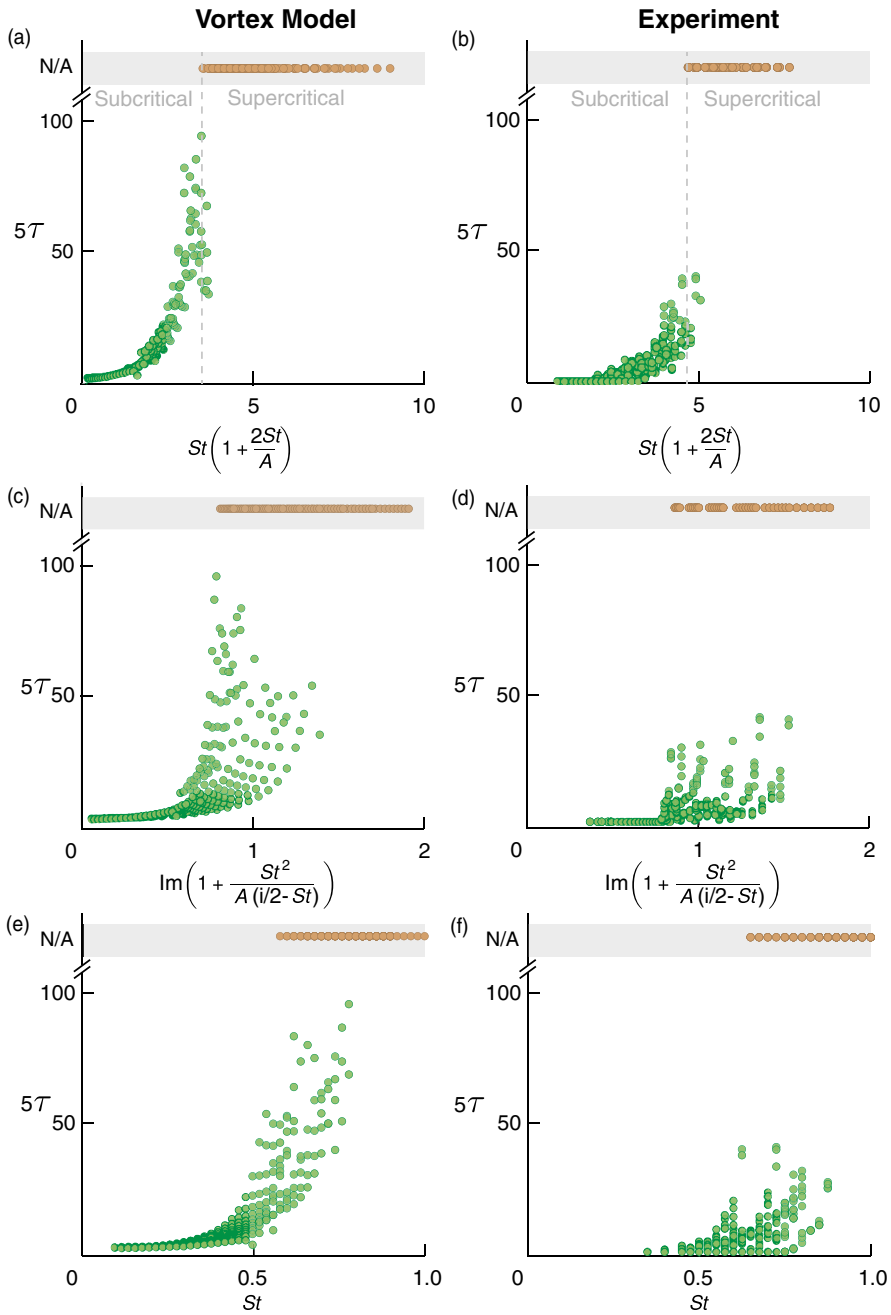


FIG. 5. Relative dipole angle scaling predicts the threshold for a deflected wake. (a), (b) Convergence times for the wake deflection angle (model) and lift coefficient (experiment) versus relative dipole angle. (c), (d) Same convergence times versus an estimate of the effective phase velocity [$\text{Im}[W_{\text{dipole}}$] in Eq. (4)]. (e), (f) Same convergence times versus the Strouhal number.

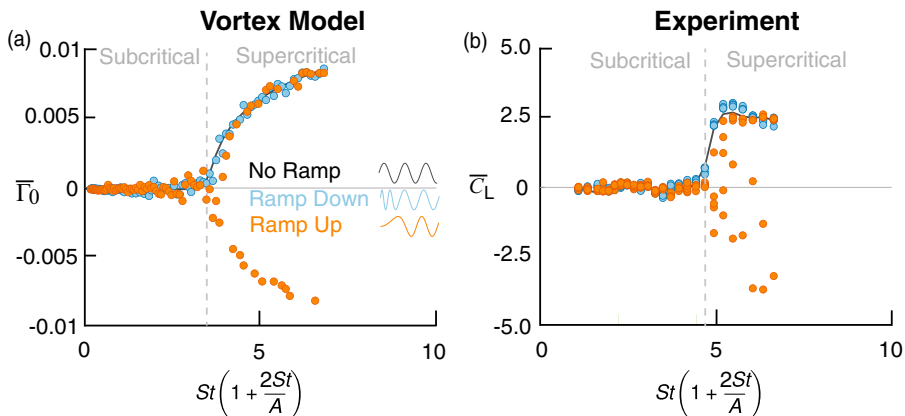


FIG. 6. Deflected wakes have minimal hysteresis. Hysteresis of the wake deflection. No Ramp: constant St ; Ramp Down: St ramps from 1 down to target value; Ramp Up: St ramps from 0 up to target value. Each data point represents an independent test trial. All trials and conditions are shown.

C. Hysteresis and bifurcation

To explore the hysteresis feature of the deflected wake, we tested a wide range of actuation motions by slowly shifting the Strouhal number up and down in both the model and the experiment (see Appendix 2). In both the model and the experiment, the transition to the deflected wake state is abrupt, with minimal hysteresis. We tested for hysteresis by checking the final states of 200-cycle ramp-down and ramp-up tests, with each trial starting with the same flapping direction. To seed the instability in the model, we added $\pm 1\%$ of Gaussian noise to the modeled flow speed u .

When $St(1 + 2St/A)$ was ramped down from ≈ 7 ($St = 1, A = 0.35$), the wake's deflection was governed by the same threshold as—and in the same direction as—the No Ramp case (Fig. 6). When $St(1 + 2St/A)$ was ramped up from 0, the wake deflected at the same threshold, but not always in the same direction [Figs. 6(c) and 6(d)]. Some cases deflected away from the initial flapping direction, as in previous work [11,14,22], but in general, the deflection direction was random. In the experiments, the wake deflection was still converging at the end of some trials, leading to scattered deflection angles and lift forces. We tested two ramp-up and ramp-down rates (± 0.25 and ± 0.05 Hz/s), and the trends were similar.

Our Ramp Down/Up results show that wake deflection is more than a lingering effect of the initial flapping direction. The C_L and $\bar{\Gamma}_0$ curves Figs. 6(c) and 6(d) imply that wake deflection undergoes a pitchfork bifurcation. With a strong initial pitch velocity (No Ramp or Ramp Down case), the system will—at super-critical conditions—tip towards a predictable branch of the pitchfork. With a weak initial pitch velocity (Ramp Up case), the branch will be determined randomly.

V. DISCUSSION

Our experiment and model corroborate the same conclusion: propulsive wakes deflect beyond a threshold relative dipole angle (θ_D). In the supercritical state, wakes deflect via a previously known mechanism [9]: each vortex pair has a positive effective phase velocity induced by the previous pairs, resulting in a perpetual asymmetry. We found that the asymmetry could be initiated by the initial flapping direction, as in previous work [11,14,22], or appear spontaneously, with no strong dependence on initial conditions.

At near-critical states, propulsive wakes converge more slowly than documented previously [5–12,14–24]. In many systems, initial conditions decay over timescales comparable to the period of forcing; here, they can decay over hundreds of oscillation cycles. Our model offers an explanation

for this feature: at near-critical θ_D values, vortex pairs have near-zero yet negative effective phase velocities [Figs. 4(b) and 4(e)], causing them to deflect just slightly less with each cycle.

Propulsive wake deflection has been considered a two-dimensional phenomenon, so its application to real propulsors may be limited. Behind three-dimensional foils, the interconnection of wake vortex loops causes most asymmetries to smooth out [12]. However, other conditions promote deflection. For example, a bias in pitch oscillations [11] or ongoing interactions with a nearby planar boundary will force a wake deflection, even with aspect ratios as small as 1 [34]. Apparently, propulsive wakes are nonlinearly unstable to deflection (Fig. 6), yet that stability can be suppressed or amplified by other factors such as three-dimensionality or asymmetric wake-boundary interactions. Even when designing three-dimensional propulsors, it may be worth considering the instability discussed here as a contributing factor to lift forces—especially when operating at high Strouhal numbers, low amplitude-to-chord ratios, or near solid boundaries.

APPENDIX

1. Additional modeling details

a. High-level description of algorithm and pseudocode

For readers interested in recreating our specific clumped vortex model, we detail the algorithm below, first using a combination of prose and pseudocode, then in Supplemental Material using the commented code of our model.

One strategy for modeling hydrofoils oscillating in an incoming flow is to use a simplified version of the Navier-Stokes equations that assumes the flow is irrotational, incompressible, and inviscid. One implementation of this simplified version is the “panel method.” In this method, vortex elements or “panels” are shed at the trailing edge every time step. Several panels may also be attached to the body to ensure no penetration (flow cannot pass through the hydrofoil), the Kelvin condition (total circulation in the system remains constant), and the Kutta condition (flow passes smoothly over the sharp trailing edge of the hydrofoil). The resulting method often gives a good approximation of flows where the main role of viscosity is to cause vortex shedding at the trailing edge; a variety of examples are given in [35].

In a “clumped vortex” model, the wake is abstracted further: instead of wake panels being shed every time step, only a few are shed per pitching cycle. This abstraction is based on the observation that in many hydrofoil wakes, vortex panels tend to roll up into vortex cores soon after being shed. One can imagine a continuum of fidelity in which wake vorticity is more and more consolidated (see, e.g., [36,28], or [31] for explorations of this continuum).

Our clumped vortex model is based in the complex plane, where distances are scaled by the hydrofoil’s chord, i.e., the hydrofoil, at its neutral position, runs from $Z = -1$ to 0 , where Z is the complex coordinate scaled by chord c and centered at the trailing edge. The hydrofoil is assumed to be pitching with an angle $\theta = \theta_0 \cos(2\pi ft)$, where θ_0 is the pitch amplitude, f is the pitch frequency, and t is time. The incoming flow speed is u . To model the circulation bound to the hydrofoil, a single vortex is kept at the quarter-chord. Because of the small amplitudes involved, the bound vortex is assumed to stay fixed to the x axis at $Z = -0.75$.

When the simulation begins, there are no wake vortices present. Then, wake vortices are “grown” at one of two positions: just downstream and either above ($Z = 0.25 + \theta_0 i$) or below ($Z = 0.25 - \theta_0 i$) the foil’s trailing edge. By grown, we mean they start at zero strength and increase in strength until they are shed when the hydrofoil achieves its maximum lateral velocity (one-quarter and three-quarters into each pitching cycle). To ensure the Kutta condition, the Kelvin condition, and the no-penetration condition, the strengths of the bound vortex and the vortex currently being grown are tuned such that no net circulation enters the system and the lateral component of the flow velocity at the “collocation point,” $Z = -0.25$, matches that of the hydrofoil. After being shed, a wake vortex’s strength does not change until it is removed from the simulation. After a user-defined maximum

number of vortices is present in the wake, the most distant vortex is scaled down slowly then deleted once per shedding cycle to improve computation efficiency.

At each time step of the simulation, four actions are taken:

(1) Calculate next bound vortex strength. The induced velocities from the bound vortex, all previously shed wake vortices, and the pitching motion are totaled at the collocation point. The strength of the bound vortex for the next time step is set such that it induces an equal and opposite lateral component, enforcing no penetration at the collocation point.

(2) Update wake vortex positions. For each shed wake vortex, the total induced velocity from all other vortices is calculated at its current position. Each vortex's position is updated for the next time step by shifting it by that induced velocity times the time-step size.

(3) Update wake vortex strengths. For the wake vortex currently growing, its strength for the next step is set to its current strength plus the current change in the bound vortex's strength. This ensures the Kelvin condition. If the wake contains the maximum number of allowed vortices, the strength of the most distant vortex is decreased based on the time elapsed since the last shedding event.

(4) Handle shedding events. If the time step corresponds to a shedding event (moment of maximum lateral velocity), the vortex currently being grown is shed, and a new wake vortex begins growing on the opposite side of the foil.

The simulation concludes when these actions have been completed a user-specified number of times.

b. Shedding time sensitivity study

The chosen shedding times (maximum lateral velocities, i.e., one-quarter and three-quarters into the pitching cycle) are user-defined inputs to the model. In a full panel code solution, the rollup of wake vortices occurs naturally. In a clumped vortex model, the rollups, and therefore the shedding times, must be prescribed based on some other criterion. What are typically chosen are the moments when the bound circulation passes through local minima and maxima. The rationale is that if the shedding occurred at any other times, then—because of the Kelvin condition—there would be a discontinuous rate of change in the strength of the wake vortex currently being grown, corresponding to a discontinuity in the force predicted on the foil. We chose the moment of maximum lateral foil velocity because it closely matches this criterion while offering a considerably simplified shedding algorithm.

The reason that maximum lateral velocity aligns with max-min bound circulation can be shown using Theodorsen's model for pitching and heaving airfoils [37]. For a harmonically pitching airfoil, the model (see, e.g., p. 397 of [35]) predicts a bound circulation of

$$\Gamma = \pi cu\theta + \frac{3\pi c^2}{4}\dot{\theta},$$

where c is the chord, u is the swimming speed, θ is the pitch angle, and dots denote time derivatives. Introducing $\theta = \theta_0 \sin(2\pi ft)$ and scaling by cu yields

$$\frac{\Gamma}{cu} = \pi \theta_0 \sin(2\pi ft) + \frac{3\pi^2 cf \theta_0}{2u} \cos(2\pi ft).$$

The first term is a circulatory component of circulation, which peaks when θ is at local maxima or minima; the second is a noncirculatory component, which peaks when $\dot{\theta}$ is at local maxima or minima. The ratio of the magnitudes of the components (noncirculatory to circulatory) is $3\pi cf/(2u)$ or $3\pi St/(2A)$, where $St = fa/u$ (a is peak-to-peak trailing edge amplitude) and $A \equiv a/c$. This ratio ranges from 7 to 47 in our dataset, so we expect the circulation to be dominated by the noncirculatory term, which peaks when lateral velocity is maximized.

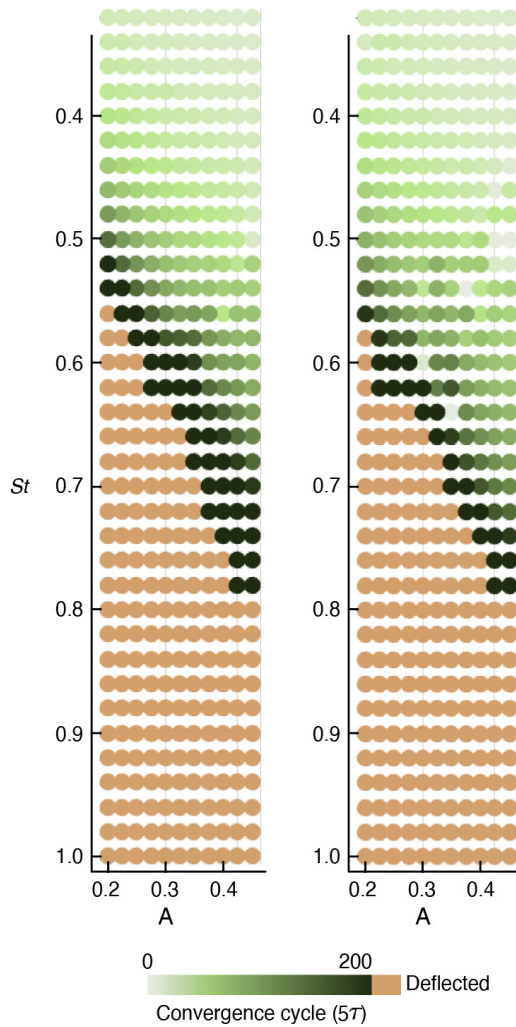


FIG. 7. Number of cycles for convergence (5τ) for the original dataset (left) and with shedding times shifted backwards by 3% of a pitch cycle (right).

To ensure that our choice did not compromise accuracy, we ran a sensitivity study on the choice of shedding time. The time histories of bound circulation showed that our shedding times occurred slightly later than the moments of minima and maxima by up to 3% of a pitch cycle. We therefore reran all of our simulations with a 3% backward shift in shedding time to explore the worst-case scenario. While there were slight changes in behavior, particularly in terms of the stability of the code with respect to time-step size, the key results of our paper were the same. Figure 7 shows the convergence results for both the original and the shifted shedding times.

c. Commented code used to run the model

Modeling was implemented in *Mathematica* 12.0.0.0 on a MacBook Pro running Mac OS 10.15.7. See the Supplemental Material [32] for commented code.

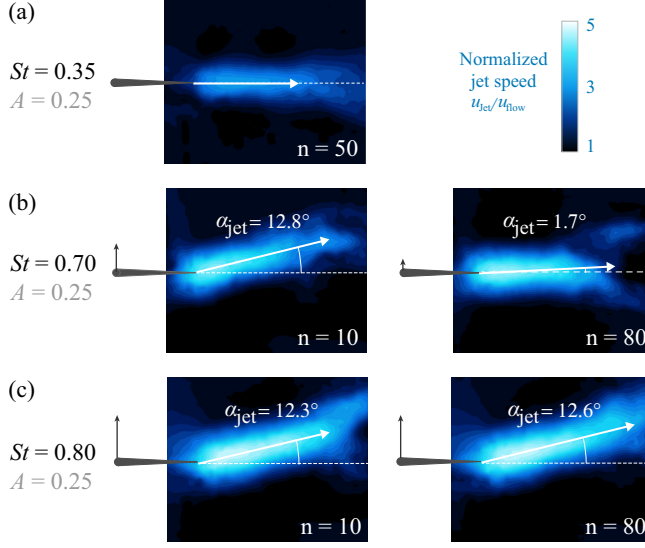


FIG. 8. Detailed cycle-averaged PIV results. Wake is calculated by cycle averaging velocity fields (ten frames) of the full pitching cycle and visualized with its normalized magnitude (u_{jet}/u_{flow}). The threshold magnitude of the wake region is 2.5.

2. Hysteresis tests

a. Experiment

To explore the hysteresis feature of the deflected wake, we tested a wide range of actuation motions to slowly shift the Strouhal number up and down. We chose to modify the Strouhal number by ramping frequency at a constant amplitude $A = 0.35$ ($\theta_0 = 10.08^\circ$). The pitching kinematics can be described by the following function:

$$\theta(t) = \begin{cases} \theta_0 \sin(2\pi f_0 t + \pi k_f t^2), & 0 \leq t \leq (f_e - f_0)/k_f \\ \theta_0 \sin(2\pi f_e t - \pi(f_e - f_0)^2/k), & t > (f_e - f_0)/k_f, \end{cases} \quad (\text{A1})$$

where f_0 is initial frequency, f_e is the target frequency, k_f is the ramping rate (Hz s^{-1}). We tested two groups that ramped up and down to target Strouhal numbers. For ramp-up cases, we set $f_0 = 0$, $k_f = 0.05 \text{ Hz s}^{-1}$, and ramps to 25 Strouhal numbers range from 0.35 ($f_e = 0.75 \text{ Hz}$) to 1.0 ($f_e = 2.14 \text{ Hz}$). For ramp-down cases, we set the same target Strouhal numbers as ramp-up cases, but set ($f_0 = 2.14 \text{ Hz}$) and $k_f = -0.05 \text{ Hz s}^{-1}$. For all test trials, we started measurements after the motion start, then measured an extra 100 cycles of steady motions after the ramping motion. We repeated each trial five times.

b. Model

When exploring hysteresis effects in the model, we modified the strengths of the first ten vortices. In the ramp-up tests, the first ten vortices ranged linearly in strength from 0 to their nominal value. In the ramp-down tests, the first ten vortices ranged linearly in strength from five times their nominal value to their nominal value.

[1] A. J. Smits, Undulatory and oscillatory swimming, *J. Fluid Mech.* **874**, P1 (2019).

[2] X. Wu, X. Zhang, X. Tian, X. Li, and W. Lu, A review on fluid dynamics of flapping foils, *Ocean Eng.* **195**, 106712 (2020).

- [3] J. B. Bratt, Flow patterns in the wake of an oscillating aerofoil, Aeronautical Research Council of United Kingdom, Tech. Rep. No. ARC/R&M-2773 (1950).
- [4] H. Lamb, *Hydrodynamics* (Cambridge University Press, Cambridge, UK, 1924).
- [5] S. Heathcote and I. Gursul, Jet switching phenomenon for a periodically plunging airfoil, *Phys. Fluids* **19**, 027104 (2007).
- [6] R. Godoy-Diana, J.-L. Aider, and J. E. Wesfreid, Transitions in the wake of a flapping foil, *Phys. Rev. E* **77**, 016308 (2008).
- [7] K. D. von Ellenrieder and S. Pothos, PIV measurements of the asymmetric wake of a two dimensional heaving hydrofoil, *Exp. Fluids* **44**, 733 (2008).
- [8] K. B. Lua, T. Lim, K. Yeo, and G. Oo, Wake-structure formation of a heaving two-dimensional elliptic airfoil, *AIAA J.* **45**, 1571 (2007).
- [9] R. Godoy-Diana, C. Marais, J.-L. Aider, and J. E. Wesfreid, A model for the symmetry breaking of the reverse Bénard–von Kármán vortex street produced by a flapping foil, *J. Fluid Mech.* **622**, 23 (2009).
- [10] C. Marais, B. Thiria, J. E. Wesfreid, and R. Godoy-Diana, Stabilizing effect of flexibility in the wake of a flapping foil, *J. Fluid Mech.* **710**, 659 (2012).
- [11] D. J. Cleaver, Z. Wang, and I. Gursul, Bifurcating flows of plunging aerofoils at high Strouhal numbers, *J. Fluid Mech.* **708**, 349 (2012).
- [12] D. Calderon, D. Cleaver, I. Gursul, and Z. Wang, On the absence of asymmetric wakes for periodically plunging finite wings, *Phys. Fluids* **26**, 071907 (2014).
- [13] X. He and I. Gursul, Point vortex model of deflected wakes of oscillating airfoils, *AIAA J.* **54**, 3647 (2016).
- [14] M. Yu, H. Hu, and Z. Wang, Experimental and numerical investigations on the asymmetric wake vortex structures of an oscillating airfoil, in *50th AIAA Aerospace Sciences Meeting Including the New Horizons 7 Forum and Aerospace Exposition, Nashville, Tennessee, USA* (AIAA, 2012), p. 299.
- [15] G. C. Lewin and H. Haj-Hariri, Modelling thrust generation of a two-dimensional heaving airfoil in a viscous flow, *J. Fluid Mech.* **492**, 339 (2003).
- [16] X. Zhang, S. Ni, S. Wang, and G. He, Effects of geometric shape on the hydrodynamics of a self-propelled flapping foil, *Phys. Fluids* **21**, 103302 (2009).
- [17] C. Liang, K. Ou, S. Premasuthan, A. Jameson, and Z. Wang, High-order accurate simulations of unsteady flow past plunging and pitching airfoils, *Comput. Fluids* **40**, 236 (2011).
- [18] Z. C. Zheng and Z. Wei, Study of mechanisms and factors that influence the formation of vortical wake of a heaving airfoil, *Phys. Fluids* **24**, 103601 (2012).
- [19] X. Zhu, G. He, and X. Zhang, How flexibility affects the wake symmetry properties of a self-propelled plunging foil, *J. Fluid Mech.* **751**, 164 (2014).
- [20] Z. Wei and Z. Zheng, Mechanisms of wake deflection angle change behind a heaving airfoil, *J. Fluids Struct.* **48**, 1 (2014).
- [21] J. Deng, L. Sun, and X. Shao, Dynamical features of the wake behind a pitching foil, *Phys. Rev. E* **92**, 063013 (2015).
- [22] M. S. U. Khalid, I. Akhtar, and N. I. Durrani, Analysis of Strouhal number based equivalence of pitching and plunging airfoils and wake deflection, *Proc. Inst. Mech. Eng., Part G: J. Aerosp. Eng.* **229**, 1423 (2015).
- [23] D. Jallas, O. Marquet, and D. Fabre, Linear and nonlinear perturbation analysis of the symmetry breaking in time-periodic propulsive wakes, *Phys. Rev. E* **95**, 063111 (2017).
- [24] N. Lagopoulos, G. Weymouth, and B. Ganapathisubramani, Universal scaling law for drag-to-thrust wake transition in flapping foils, *J. Fluid Mech.* **872**, R1 (2019).
- [25] K. Jones, C. Dohring, and M. Platzer, Experimental and computational investigation of the Knoller-Betz effect, *AIAA J.* **36**, 1240 (1998).
- [26] C. E. Brown Jr. and W. Michael, Effect of leading-edge separation on the lift of a delta wing, *J. Aeronaut. Sci.* **21**, 690 (1954).
- [27] S. Michelin, S. G. L. Smith, and B. J. Glover, Vortex shedding model of a flapping flag, *J. Fluid Mech.* **617**, 1 (2008).

- [28] J. Sheng, A. Ysasi, D. Kolomenskiy, E. Kanso, M. Nitsche, and K. Schneider, Simulating vortex wakes of flapping plates, *Natural Locomotion in Fluids and on Surfaces: Swimming, Flying, and Sliding* (Springer, New York, 2012), pp. 255–262.
- [29] A. U. Oza, L. Ristroph, and M. J. Shelley, Lattices of hydrodynamically interacting flapping swimmers, *Phys. Rev. X* **9**, 041024 (2019).
- [30] C. Wang and J. D. Eldredge, Low-order phenomenological modeling of leading-edge vortex formation, *Theor. Comput. Fluid Dyn.* **27**, 577 (2013).
- [31] J. D. Eldredge, *Mathematical Modeling of Unsteady Inviscid Flows* (Springer, New York, 2019), Vol. 50.
- [32] See Supplemental Material at <http://link.aps.org/supplemental/10.1103/PhysRevFluids.9.064702> for our step-by-step algorithm and commented source code.
- [33] D. Cleaver, Z. Wang, and I. Gursul, Investigation of high-lift mechanisms for a flat-plate airfoil undergoing small-amplitude plunging oscillations, *AIAA J.* **51**, 968 (2013).
- [34] Q. Zhong, T. Han, K. W. Moored, and D. B. Quinn, Aspect ratio affects the equilibrium altitude of near-ground swimmers, *J. Fluid Mech.* **917**, A36 (2021).
- [35] J. Katz and A. Plotkin, *Low-Speed Aerodynamics* (Cambridge University Press, Cambridge, UK, 2001), Vol. 13.
- [36] D. Darakananda and J. D. Eldredge, A versatile taxonomy of low-dimensional vortex models for unsteady aerodynamics, *J. Fluid Mech.* **858**, 917 (2019).
- [37] T. Theodorsen, General theory of aerodynamic instability and the mechanism of flutter, Tech. Rep. No. NACA-TR-496 (1949).